Received: 25 August 2016 | Revised: 20 March 2017 | Accepted: 24 March 2017

DOI: 10.1002/gj.2943

WILEY

RESEARCH ARTICLE

Fluid inclusion and isotope geochemistry of the Atebayue Sb deposit, South Tianshan Orogen, Kyrgyzstan

Zhenju Zhou[1,2] | Zhengle Chen[1] | Fengbin Han[1] | Shuqin Han[1] | Zongxiu Wang[1] | Weifeng Xiao[1] | Tao Shen[3] | Junjie Wu[3]

[1] Institute of Geomechanics, Chinese Academy of Geological Sciences, Beijing, China

[2] Key Laboratory of Orogen and Crustal Evolution, Peking University, Beijing, China

[3] State Key Laboratory of Nuclear Resources and Environment, East China Institute of Technology, Nanchang, China

Correspondence
Z.L. Chen, Institute of Geomechanics, Chinese Academy of Geological Sciences, Beijing, 100081, China.
Email: chenzhengle@263.net; 156042284@qq.com

Funding information
National Natural Science Foundation of China, Grant/Award Number: U1403292 and 41402061

Handling editor: I. Somerville

The Atebayue Sb deposit is hosted in the Silurian clastics in the South Tianshan Orogen in Kyrgyzstan. The Sb ores appear as veins/veinlets and disseminations, with stibnite being the main ore mineral. Gangue minerals comprise quartz, calcite, and clay minerals. The quartz at Atebayue only contains aqueous fluid inclusions with low homogenization temperature (215–336 °C) and salinity (3.4–6.9 wt.% NaCl equiv.), supporting an epizonogenic hydrothermal origin. The minimum trapping pressures estimated from the NaCl—H_2O inclusions are 9–14 MPa, suggesting that the Sb mineralization mainly occurred at a depth of 0.9–1.4 km. Sulphur isotopes ($\delta^{34}S$ = −0.4 to 6.2‰) suggest that the host rocks within the Silurian system to be a significant source of ore metals. The ores contain average $^{206}Pb/^{204}Pb$, $^{207}Pb/^{204}Pb$, and $^{208}Pb/^{204}Pb$ values of 18.112, 15.547, and 38.064, respectively, and 2-stage model ages of 337–381 Ma, indicating the ores were likely sourced from the Paleozoic strata. Integrating the data obtained from the studies including ore geology, fluid inclusion, and S—Pb isotope geochemistry, we conclude that that the Atebayue Sb deposit is best classified as epizonogenic type formed by the Tarim–Kazakhstan continent–continent collision.

KEYWORDS

Atebayue Sb deposit, fluid inclusion, isotope geochemistry, Kyrgyzstan, South Tianshan Orogen

1 | INTRODUCTION

The South Tianshan Orogen, which extends across Uzbekistan, Tajikistan, eastern Kazakhstan, Kyrgyzstan, and Xinjiang (NW China), is the most important Hg—Sb mineral province in the world and contains a proven reserve of over 5 Mt Sb and 0.8 Mt Hg (Li, Qiu et al., 2010). The orogen also contains significant Au, Pb, Zn, Al, Sn, and W endowment, such as the world's largest Muruntau orogenic Au deposit (Goldfarb, Taylor, Collins, Goryachev, & Orlandini, 2014), the Huoshibulake MVT Pb—Zn deposit (Li, Xue, Zhang, Shi, & Wang, 2010), the large Boruhskoe and Hodgaachkan Al deposits, the large Uchkochkon Sn and Trudovoe W—Sn deposits, and the Meliksu and Kumysh-Tash W deposits (Li, Qiu et al., 2010; Yao et al., 2015). Located on the northern margin of the Tarim Craton (TC), the South Tianshan Orogen is an important component of the southwestern part of the Central Asia Orogenic Belt (CAOB; Sengör, Natalin, & Burtman, 1993). The South Tianshan experienced a long-lived arc-basin evolution and had formed abundant Hg—Sb—Au deposits but no important porphyry and skarn Cu deposits, a feature different from the Middle and Northern Tianshan in the CAOB (Chen, Zhou et al., 2012c). Although this unique feature and the economic significance have led to many recent investigations (e.g., Belousov, 2002; Chen & Jing, 2012; Li, Qui et al., 2010; Osmonbetov, 1986; Yao et al., 2015), the fluid source and genesis of the South Tianshan Hg—Sb deposits remain variably attributed to: (a) clastic rock type (Yao et al., 2015); (b) carbonatite type (Yao et al., 2015); and (c) magmatic-hydrothermal type (Li, Qui et al., 2010).

Scientific research on the newly discovered Atebayue deposit (in the Atbashi Hg—Sb orefield) is very limited. In this paper, we report new ore geology, fluid inclusion, and S—Pb isotope data of the Atebayue deposit and discuss the nature of the ore–fluid system at Atebayue, as well as the deposit type and probable tectonic setting.

2 | REGIONAL GEOLOGY

The South Tianshan Orogen (about 2,500 km long) is bounded by the Talas-Fergana and Atbashi-Inylchek faults to the north and the south Fergana Fault to the south (Figure 1a,b) and records the final collision between the Tarim and Siberian cratons (Sengör et al., 1993).

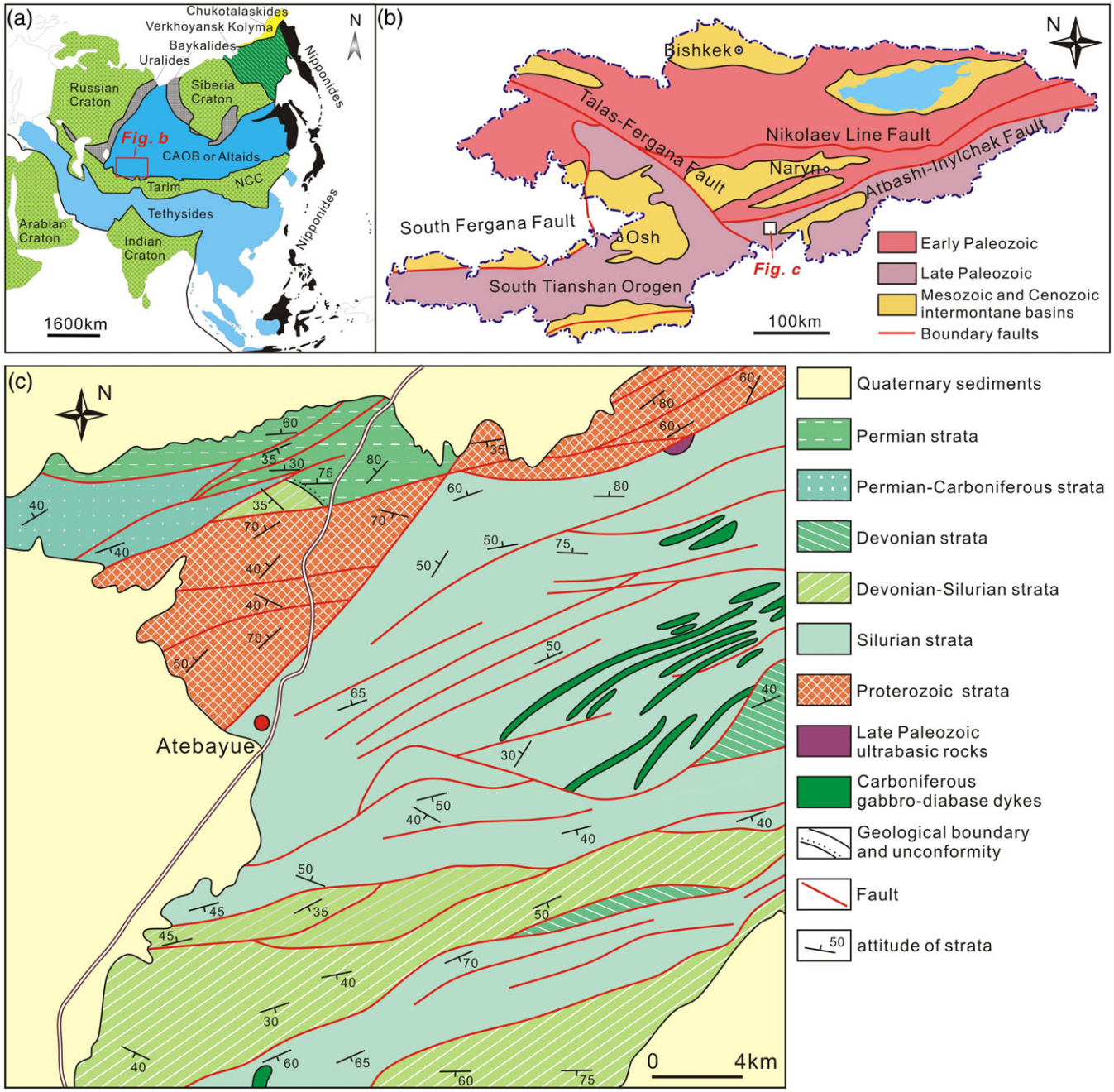

FIGURE 1 (a) Schematic map showing the location of Kyrgyzstan (modified after Sengör et al., 1993). Abbreviation: CAOB = Central Asia Orogenic Belt; NCC = North China Craton; (b) tectonic subdivision of Kyrgyzstan, showing the location of the Atbashi Hg—Sb orefield; (c) geologic map of the Atbashi Hg—Sb belt [Colour figure can be viewed at wileyonlinelibrary.com]

The Atbashi Hg—Sb orefield is located in the eastern part of the South Tianshan Orogen (Figure 1b). The orefield is well developed within the Proterozoic and Palaeozoic strata. The Proterozoic system is mainly composed of metamorphosed schist and marble. The Silurian strata is characterized by clastic sediments, consisting of limestone, sandstone, shale, marble, siliceous mudstone, and tuff. The Silurian–Devonian strata comprise limestone. The Devonian strata consists mainly of limestone, shale, and sandstone. The Carboniferous–Permian strata are mainly composed of sandstone, siltstone, and limestone, whilst the Permian strata comprise mainly conglomerate, mudstone, and limestone.

Faults and tight folds are well developed in the Palaeozoic strata in this area and are dominantly NE-, ENE-, and E-W-trending. The NE- or E–W-trending Atbashi-Inylchek Fault is a large sinistral strike-slip fault (over 500 km long), and its subsidiary faults are likely a major ore-controlling structure for the Atbashi Hg—Sb orefield (Figure 1b,c). The only intrusive rocks in the area are the ENE-trending Carboniferous gabbro–diabase dykes in the eastern and southern parts of the mining district.

3 | LOCAL AND ORE GEOLOGY

Exposed stratigraphy at Atebayue is mainly Proterozoic, Silurian, and Quaternary (Figures 2 and 3). The Proterozoic strata comprise mainly crystalline schist and marble. The Silurian Lower Ludebuofu Group consists of low-grade metamorphosed clastics, including schist,

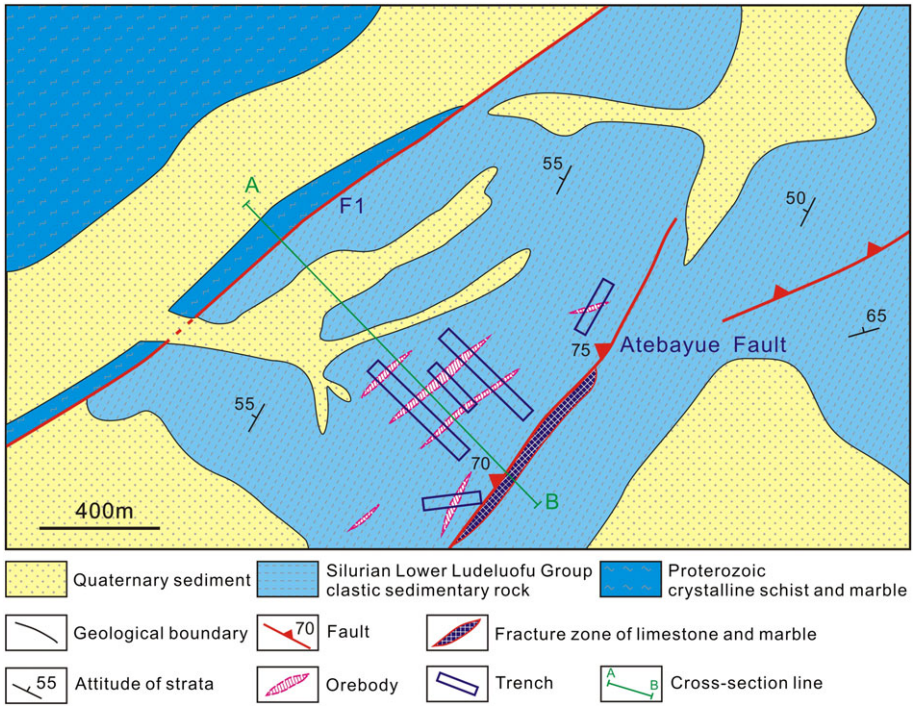

FIGURE 2 Geological map of the Atebayue. Sb deposit [Colour figure can be viewed at wileyonlinelibrary.com]

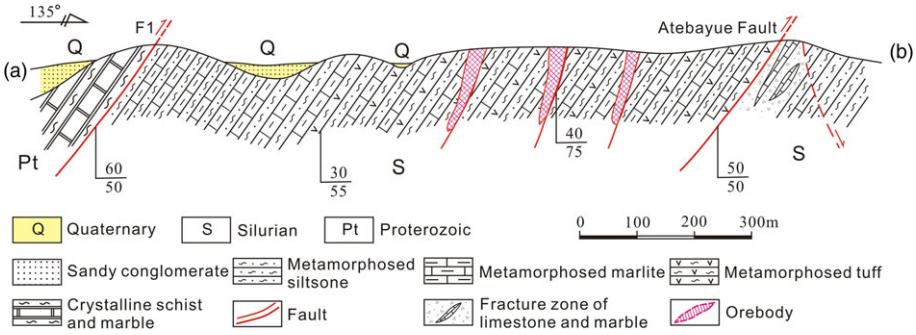

FIGURE 3 Geological cross-section (a-b in Figure 2) of the Atebayue Sb deposit [Colour figure can be viewed at wileyonlinelibrary.com]

metamorphosed marlite, siltstone, sandstone and tuff, and marble. Structures at Atebayue are dominated by the NNE-trending Atebayue Fault and its subsidiary structures (Figures 2 and 3). Due to their new discovery, there is no detailed information about the Atebayue Sb orebodies. According to our field and trench observation, the orebodies are commonly hosted in the hanging wall of the subsidiary structures of the Atebayue Fault.

The Atebayue deposit contains six small orebodies, which are mainly NE-trending (45–50°) and minor ENE-trending (65–70°) or NNE-trending (20–30°), and steeply (80–90°) SE-dipping. The orebodies are generally 100 to 200 m long and 1 to 2 m thick. The Sb ore is hosted mainly in brecciated quartz veins (Figure 2) with the metallic minerals being mainly stibnite (Figure 4) with minor pyrite and marcasite. The gangue minerals are predominately quartz, calcite, and clay minerals.

Based on the ore morphology, texture, and paragenesis, two types of stibnite are recognized (Figure 4a). Stibnite 1 is medium-grained (0.2 to 0.8 mm in diameter), subhedral to anhedral columnar (Figure 4b,c). Many Stibnite 1 grains are broken or brecciated (Figure 4d) and replaced by quartz. Stibnite 1 usually coexists with pyrite and marcasite (Figure 4e). Pyrite (0.01 to 0.08 mm in diameter) is subhedral or anhedral (Figure 4f), whilst marcasite is usually euhedral to subhedral and occurs as radial aggregates (Figure 4e). Stibnite 2 is fine-grained (0.02 to 0.1 mm in diameter) and dominantly euhedral to subhedral. It occurs in veinlets (Figure 4g) or stockwork (0.01 to 0.05 mm wide) and locally shows rhythmic banding (Figure 4h) or corrugation (Figure 4i). The ores appear as disseminated, brecciated, stockwork, vein, or veinlet (Figure 4a). Ore textures include mainly open-space filling (Figure 4e,h,i), dissemination, metasomatic remnant/embayment (Figure 4h), and replacement. Drusy and vuggy textures and geodes are commonly observed. Alteration styles are dominated by silicification, and pyritization, followed by carbonation.

4 | SAMPLES AND ANALYTICAL METHODS

4.1 | Fluid inclusion study

Doubly polished thin sections (~0.20 mm thick) were prepared from 13 ore samples. Fluid inclusions were carefully observed to identify their

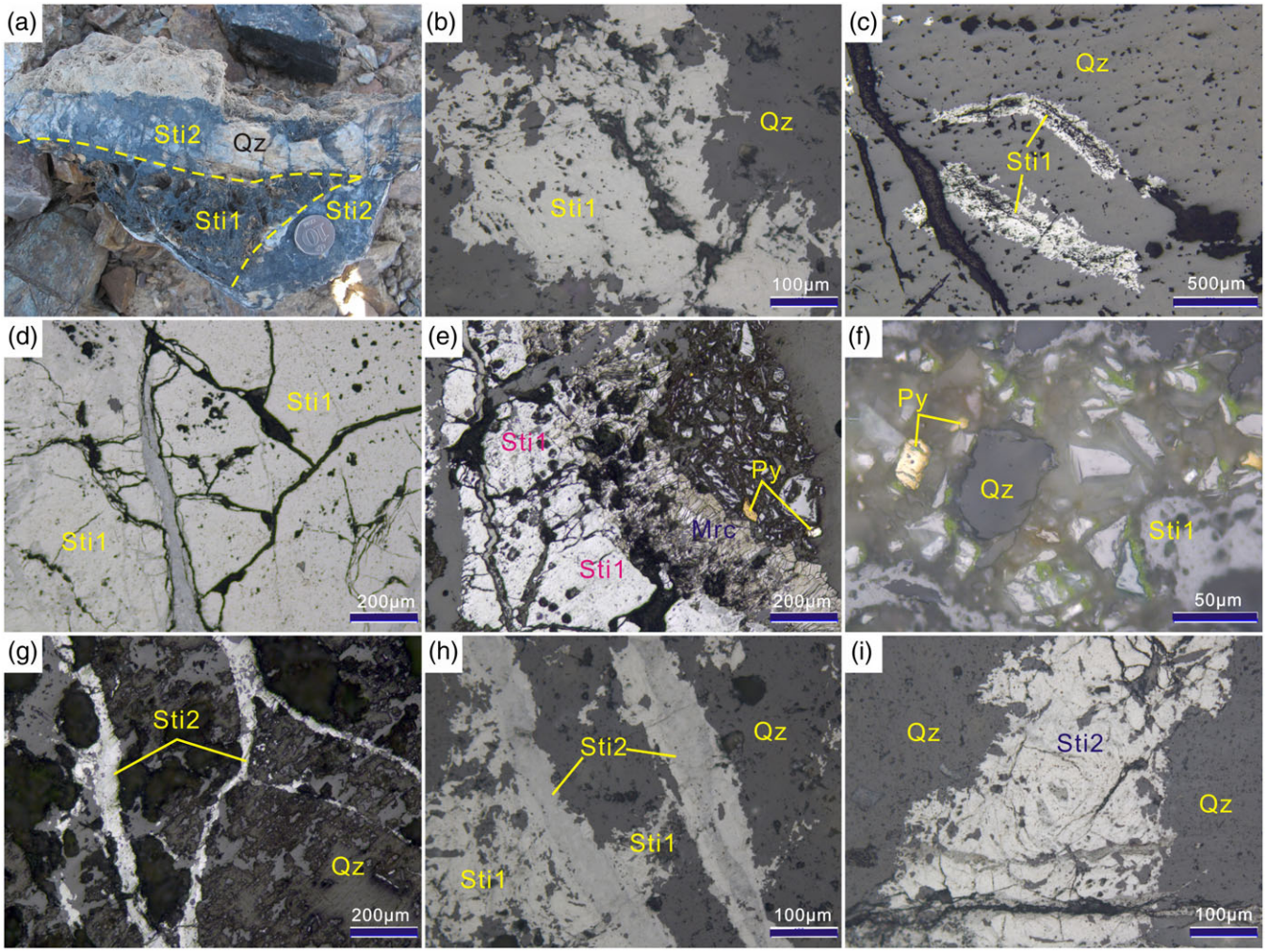

FIGURE 4 Hand specimen and thin section (reflected light) photographs of the Atebayue Sb deposit. (a) Stibnite 1 (Sti1) and Stibnite 2 (Sti2) associated with quartz; (b) medium-grained subhedral to anhedral stibnite; (c) columnar stibnite; (d) broken stibnite; (e) coexisting stibnite, pyrite, and marcasite radial aggregates; (f) subhedral to anhedral pyrite; (g) fine-grained euhedral to subhedral stibnite veinlets; (h) Sti1 and rhythmic banded Sti2; (i) corrugated stibnite. Abbreviations: Sti = stibnite; Py = pyrite; Mrc = marcasite; Qz = quartz [Colour figure can be viewed at wileyonlinelibrary.com]

genetic types, vapour–liquid ratios, and spatial clustering (Figure 5). Five representative samples were selected for microthermometric measurements and laser Raman spectroscopy analyses.

Microthermometric measurements were performed at the Institute of Geomechanics, Chinese Academy of Geological Sciences (CAGS Beijing), using a Linkam THMSG 600 heating–freezing stage, which is attached to a Leitz Ortholux transmitted light microscope connected to a television camera and screen. The stage was calibrated using synthetic fluid inclusions. The estimated accuracy was ±0.1 °C at temperatures below 30 °C and ±1 °C at temperatures above 30 °C. The warming rate was maintained at 0.2 to 5 °C per minute, and the heating rate was reduced to 0.2 °C per minute when close to phase-change conditions. Freezing experiments were performed first on all sections to avoid inclusion decrepitation. The measured phase transitions include the ice-melting temperature ($T_{m\text{-}ice}$) and the total mineralization temperature (T_h). Salinities were calculated using the equations of Bodnar (1993) for aqueous fluids.

The composition of a single fluid inclusion, including vapour and liquid phases, was determined using a LabRam HR Laser Raman microspectrometer at the Key Laboratory of Mineral Resources, Institute of Geology and Geophysics, China Academy of Sciences (CAS). The analysis used an argon ion laser with wavelength of 532 nm and the measured spectrum time of 20 s. Counting rate was one time per centimeters, and the spectral range falls between 100 and 4,000 cm^{-1}.

Bulk ion compositions of fluid inclusions were determined at the Key Laboratory of Mineral Resources, Institute of Geology and Geophysics, CAS. The gas and liquid concentrations of the fluid inclusions were extracted using the decrepitation method and then measured with a Prisma TM QMS200 quadrupole mass spectrometer and a HIC-6A ion chromatograph for gas and liquid compositions, respectively.

4.2 | Isotope analysis

Six stibnite samples have been analysed for sulphur and lead isotopic compositions at the Analytical Laboratory of the Beijing Research Institute of Uranium Geology. Minerals separates were extracted from crushed and washed sample fragments and were selected by handpicking under a binocular microscope to achieve >99% purity.

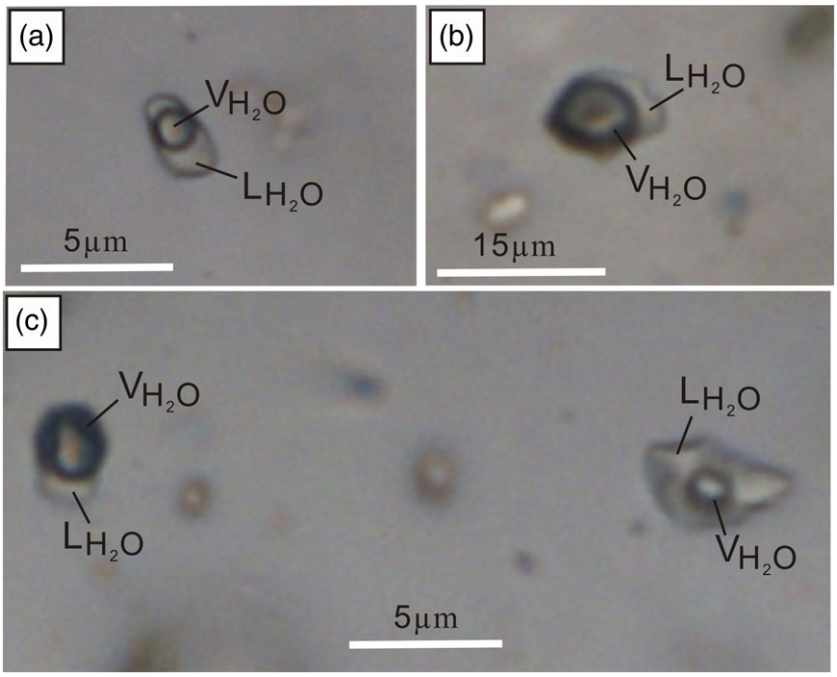

FIGURE 5 Photomicrographs of fluid inclusions in quartz from the Atebayue Sb deposit. (a) Liquid-rich aqueous inclusion in quartz; (b) vapour-rich aqueous inclusion in quartz; (c) W-type fluid inclusions with various vapour/liquid ratios in quartz. Abbreviation: V_{H2O} = vapour H_2O; L_{H2O} = liquid H_2O [Colour figure can be viewed at wileyonlinelibrary.com]

For the sulphur isotope analysis, each sample was weighed to 15 mg, mixed with CuO powder, placed in a vacuum quartz tube, and allowed to react for 15 min at a temperature of 1,100 °C (Robinson & Kusakabe, 1975). After purification, SO_2 was transferred to the sample tube, and the $^{34}S/^{32}S$ ratio was measured with a Finnigan MAT 251 mass spectrometer. The isotope data were reported in per mil relative to the Canyon Diablo Troilite (CDT) standard. The reproducibility of $\delta^{34}S$ values was ±0.2‰. The lead isotopic ratios were determined using a GV IsoProbe-T multicollector thermal ionisation mass spectrometer (TIMS). The Pb-isotope analysis results were reported with respect to the Pb standard reference NBS-981 values (Todt, Cliff, Hanser, & Hofmann, 1993): $^{206}Pb/^{204}Pb$ = 16.934 ± 0.007, $^{207}Pb/^{204}Pb$ = 15.486 ± 0.012, and $^{208}Pb/^{204}Pb$ = 36.673 ± 0.033, respectively. Analytical precision was better than ±0.005%. Isotope data are presented in Tables 3 and 4.

5 | RESULTS

5.1 | Fluid inclusion microthermometry

Petrographic and microthermometric studies show that the quartz contains only aqueous inclusions (W-type), with most of them showing two phases (L_{H2O} + V_{H2O}) at room temperature (Figure 5). This is in agreement with the Laser Raman spectroscopic detection results that the vapour and liquid phases in any of the fluid inclusions (FIs) are dominated by H_2O (Figure 6). According to the vapour/liquid ratio in volume, the FIs can be further divided into liquid-rich (vapour/liquid <50 vol.%; Figure 5a) and vapour-rich (vapour/liquid >50 vol.%; Figure 5b), with the former being more common (Figure 5c). Morphologically, the fluid inclusions (2 to 15 μm in size) are subrounded to oval or irregularly shaped. The primary W-type FIs are isolated or randomly distributed, and the secondary W-type FIs are mostly irregularly shaped and occur along healed fractures. The FIs are totally homogenised to liquid at 215–336 °C (T_h), peaking at 260–300 °C (Figure 7). The vapour- and liquid-rich FIs generally show similar T_h values. Their $T_{m\text{-}ice}$ range from −2.0 to −4.3 °C (Table 1).

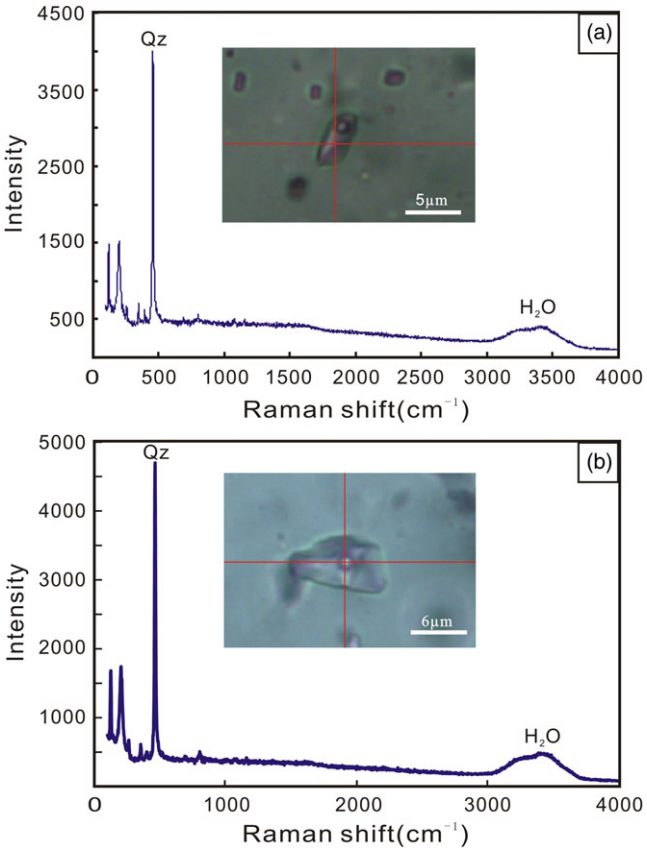

FIGURE 6 Representative Raman spectra of fluid inclusions of the Atebayue Sb deposit. (a) Liquid phase in aqueous inclusions in quartz (Qz) containing water only; (b) vapour bubbles of aqueous inclusions in quartz, containing H_2O only [Colour figure can be viewed at wileyonlinelibrary.com]

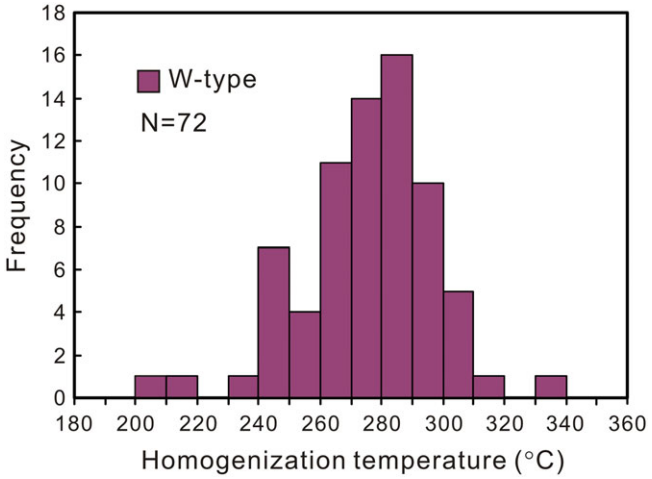

FIGURE 7 Histogram of homogenization temperatures of the fluid inclusions in quartz [Colour figure can be viewed at wileyonlinelibrary.com]

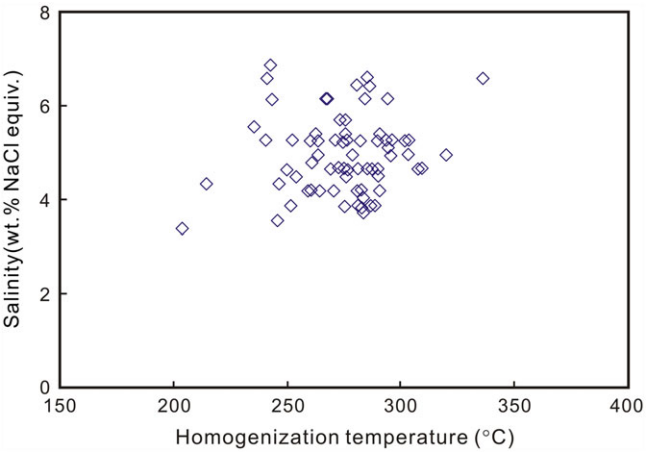

FIGURE 8 Diagram of homogenization temperature versus salinity of fluid inclusions [Colour figure can be viewed at wileyonlinelibrary.com]

corresponding to salinities between 3.4 and 6.9 wt.% NaCl equiv. (Figure 8). These results show that the ore-forming fluids were of low temperature and low salinity. Because only W-type FIs were found, we used W-type FIs with the NaCl—H_2O P-T-X diagram to estimate the mineralization pressure (Bouzari & Clark, 2006). The minimum trapping pressure of FIs at Atebayue was 9–14 MPa (Figure 9). The pressure of the fluid system was hydrostatic, with the depth calculated to be 0.9–1.4 km. Hence, we conclude that the Atebayue Sb mineralization may have occurred at the shallow crust (<2 km). The depth overlaps that of many major Hg—Sb deposits worldwide (0.7–6 km; Chen, 2006, 2013; Groves, Goldfarb, Gebre-Mariam, Hagemann, & Robert, 1998).

5.2 | Bulk volatile and ion composition

Bulk molecule and ion compositions of the fluids trapped in quartz are listed in Table 2. Except for O_2 and H_2S, five volatile compositions (H_2O, N_2, Ar, CO_2, and CH_4) were detected in all samples. C_2H_6 only occurs in samples KG1302-1A, KG1302-1C, KG1302-1E, and KG1302-1F. H_2O is the dominant composition, consistent with the laser Raman spectroscopic results. KG1302-1A has the highest CO_2, N_2, and C_2H_6. Two anion (Cl^- and SO_4^{2-}) and three cation (Na^+, K^+, and Ca^{2+}) types were detected by the bulk ion analysis (Table 2). In general, the Cl^-, Na^+ and Ca^{2+} contents are much higher than the SO_4^{2-} and K^+ contents in quartz. No F^- and Mg^{2+} were identified in the quartz. Bulk gas and ion composition analyses show that the fluid inclusions commonly contain H_2O, CO_2, CH_4, N_2, and Ca^{2+} and locally C_2H_6, SO_4^{2-}, and K^+, which indicate the presence of a complex fluid system rather than a simple "H_2O + NaCl" fluid composition.

5.3 | Sulphur isotope

The stibnite $\delta^{34}S$ values from the Atebayue deposit range from −0.4 to 6.2‰ (average: 2.3‰; Table 3 and Figure 10), similar to those (−9 to 10‰) of the other Southern Tianshan Hg—Sb deposits (Figure 10; Wang, Jin, Bao, Sha, & Hu, 2003; Yao et al., 2015). The Atebayue stibnite $\delta^{34}S$ values are also comparable to those of most lode Hg—Sb deposits in Qinling, such as the Xunyang Hg—Sb orefield (−6.4 to 11.8‰; Bai & Zhu, 1984; Ding, 1986; Yang, 1991; Zhang, Tang, Chen, Leng, & Zhao, 2014), in which the sulphur was likely sourced from the ore-hosting strata. Some sulphides in sediment-hosted deposits could be significantly ^{34}S enriched (Sasaki & Krouse, 1969). The high $\delta^{34}S$ values (6.2‰) of some Atebayue stibnite samples suggest significant sedimentary wall rock contribution (Hoefs, 1997), whereas the other three stibnite samples with near-zero ^{34}S values (−0.4 to −0.6) likely indicate that a magmatic sulphur source was also present (Hoefs, 1997).

5.4 | Lead isotope

The Atebayue Sb ores have $^{206}Pb/^{204}Pb$, $^{207}Pb/^{204}Pb$, and $^{208}Pb/^{204}Pb$ values of 18.049–18.173 (average: 18.112), 15.561–15.599 (average: 15.547), and 37.994–38.167 (average: 38.064; Table 4), respectively. In Figure 11, the Atebayue Pb isotope data plot near the orogen line (Zartman & Doe, 1981), showing the complexities of

TABLE 1 Microthermometric data for fluid inclusions in quartz from the Atebayue Sb deposit

Sample no.	Type	Number	Size (μm)	Vapor (vol.%)	$T_{m\text{-}ice}$ (°C)	T_h (°C)	Salinity (wt.% NaCl equiv.)
KG1302-1F	W	21	4–10	5–65	−2.0 to −4.1	204–336	3.4–6.6
KG1302-2B	W	9	4–6	10–40	−2.4 to −4.1	273–310	4.0–6.6
KG1302-2C	W	11	4–6	5–60	−2.5 to −3.8	235–295	4.2–6.2
KG1302-2D	W	15	4–8	5–70	−2.3 to −4.1	241–290	3.9–6.6
KG1302-1D	W	16	4–12	10–90	−2.2 to −4.3	243–294	3.7–6.9

Note. $T_{m\text{-}ice}$ = ice-melting temperature; T_h = total homogenization temperature.

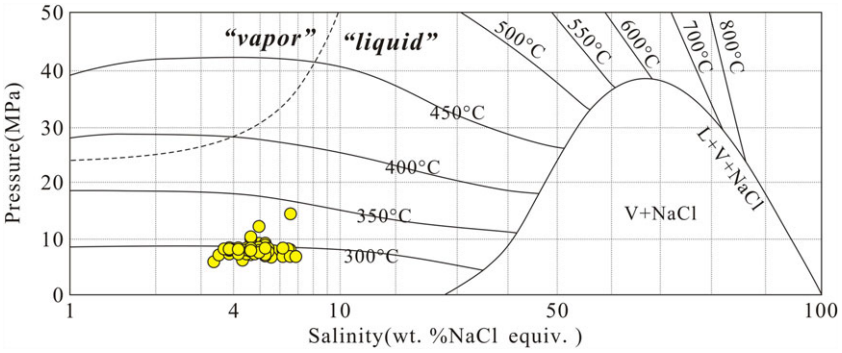

FIGURE 9 Estimated pressure for the fluid inclusions in quartz from the Atebayue Sb deposit (modified after Bouzari & Clark, 2006) [Colour figure can be viewed at wileyonlinelibrary.com]

TABLE 2 Bulk volatile (mol%) and aqueous (μg/g) compositions of in Atebayue Sb deposit

Samples	KG1302–1A	KG1302–1B	KG1302–1C	KG1302–1D	KG1302–1E	KG1302–1F	KG1302–2A	KG1302–2B	KG1302–2C	KG1302–2D
H_2O	75.81	96.11	98.02	96.53	94.98	98.42	98.45	99.01	98.10	99.24
N_2	0.35	0.11	0.06	0.09	0.10	0.04	0.08	0.09	0.10	0.07
Ar	0.02	0.02	0.01	0.01	0.01	0.01	0.02	0.03	0.02	0.02
O_2	b.d	b.d	b.d	b.d	b.d	b.d	b.d	b.d	b.d	b.d
CO_2	23.55	3.64	1.81	3.30	4.78	1.46	1.35	0.68	1.65	0.56
CH_4	0.09	0.13	0.08	0.08	0.09	0.06	0.11	0.19	0.14	0.12
C_2H_6	0.16	0.00	0.02	0.00	0.04	0.01	0.00	0.00	0.00	0.00
H_2S	b.d	b.d	b.d	b.d	b.d	b.d	b.d	b.d	b.d	b.d
F^-	b.d	b.d	b.d	b.d	b.d	b.d	b.d	b.d	b.d	b.d
Cl^-	0.60	0.53	1.99	0.90	0.53	2.55	1.20	0.53	0.54	0.42
SO_4^{2-}	b.d	1.74	b.d	b.d	1.58	b.d	b.d	b.d	b.d	0.49
Na^+	0.32	0.69	1.24	1.28	0.56	1.58	0.93	0.92	0.41	0.44
K^+	b.d	b.d	b.d	b.d	b.d	b.d	b.d	b.d	b.d	0.37
Mg^{2+}	b.d	b.d	b.d	b.d	b.d	b.d	b.d	b.d	b.d	b.d
Ca^{2+}	0.57	0.48	0.46	0.34	0.51	0.46	0.40	0.34	0.46	0.30

Note. b.d = below the detection.

TABLE 3 The $\delta^{34}S$ values of ores at the Atebayue Sb deposit

No.	Sample description	Sample no.	Mineral	$\delta^{34}S$
1	Ore	KG1302-1A	Stibnite	−0.4
2	Ore	KG1302-1B	Stibnite	−0.5
3	Ore	KG1302-1C	Stibnite	−0.6
4	Ore	KG1302-1D	Stibnite	3.6
5	Ore	KG1302-1E	Stibnite	5.4
6	Ore	KG1302-1F	Stibnite	6.2
		Average		2.3

possible Pb sources. The stibnite Pb isotopes yielded two-stage model ages of 337–381 Ma, suggesting that the metals were likely sourced from the Palaeozoic strata (Figure 1c).

6 | DISCUSSION

6.1 | Ore deposit type

Major geological and geochemical features of the Atebayue Sb deposit include:

1. The deposit is hosted in Silurian strata, which are structurally deformed (tightly folded) and locally metamorphosed (up to low-grade greenschist facies).
2. The quartz ore veins are distinctly controlled by brittle faults, suggesting that the mineralization depth was shallow (<10 km; Chen, 2010), as also supported by our new fluid inclusion evidence (<2 km).
3. The orefield is distant from known magmatic (especially granitoid) bodies (Figure 1c), but close to other South Tianshan low-temperature hydrothermal mineral systems such as barite (Yang, Mao, Wang, & Bierlein, 2006), sediment-hosted U (Chen, Zhou et al., 2012c), Carlin-like (Goldfarb et al., 2014) and MVT Pb-Zn (Xue et al., 2014; Zhu, Wang, Liu, & Fang, 2010).
4. Antimony mineralization-related alteration styles include mainly silicification, and sulphidization, and local carbonation, which are common in low-temperature hydrothermal systems (Chen et al., 2007; Pirajno, 2009; Tu, 1998).
5. Metallic mineral assemblage (stibnite > pyrite + marcasite) is typical of low-temperature hydrothermal systems. Open-space filling veins and stockworks with drusy, zigzag, and vuggy structures,

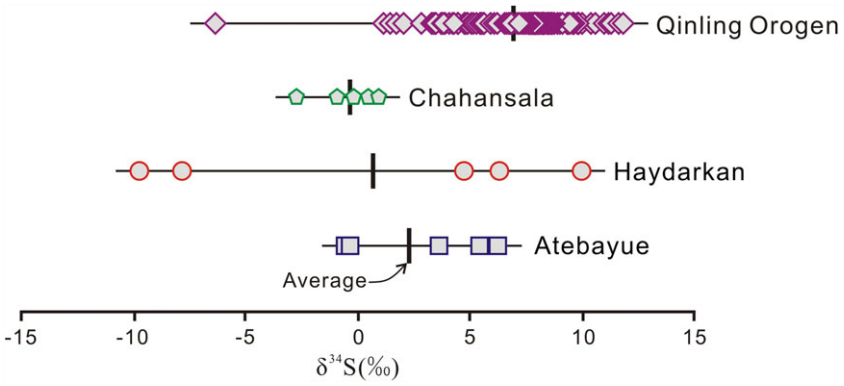

FIGURE 10 $\delta^{34}S$ values of sulphides from the Atebayue deposit. Data sources of other deposits are given in the text [Colour figure can be viewed at wileyonlinelibrary.com]

TABLE 4 Lead isotope ratios of ores at the Atebayue Sb deposit

No.	Sample description	Sample no.	Testing object	$^{206}Pb/^{204}Pb$	$^{207}Pb/^{204}Pb$	$^{208}Pb/^{204}Pb$
1	Ore	KG1302-1A	Stibnite	18.097	15.571	38.079
2	Ore	KG1302-1B	Stibnite	18.173	15.599	38.167
3	Ore	KG1302-1C	Stibnite	18.094	15.567	37.996
4	Ore	KG1302-1D	Stibnite	18.116	15.568	38.054
5	Ore	KG1302-1E	Stibnite	18.141	15.579	38.091
6	Ore	KG1302-1F	Stibnite	18.049	15.561	37.994
		Average		18.112	15.574	38.064

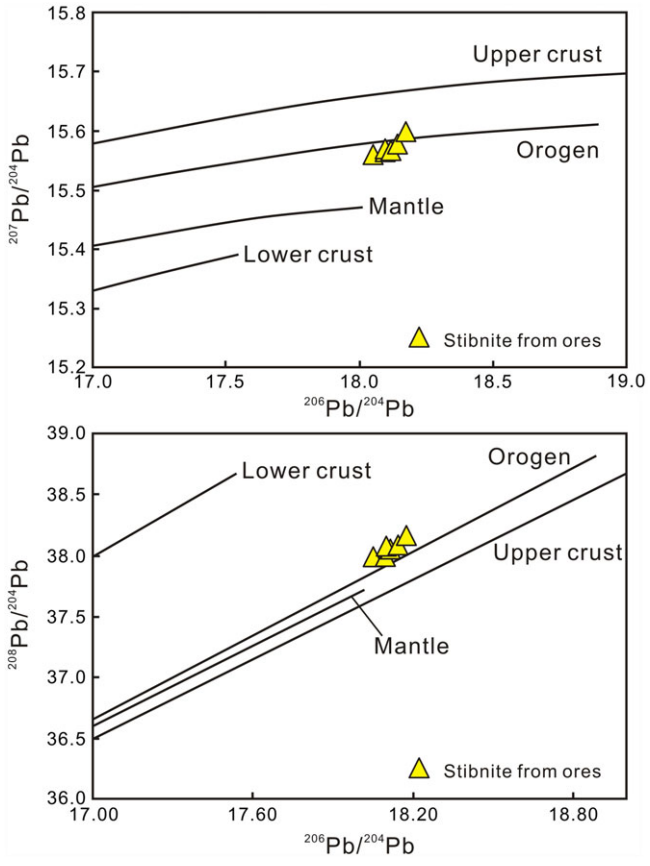

FIGURE 11 Lead isotope compositions of the Atebayue deposit (modified after Zartman & Doe, 1981) [Colour figure can be viewed at wileyonlinelibrary.com]

as well as the geodes in veins or altered tectonite zone, strongly indicate an epizonogenic mineralization.

6. The microthermometric, laser Raman spectroscopic, and bulk volatile and ion composition data suggest that the fluid system was dominated by liquid-rich NaCl—H_2O, with minor CO_2, CH_4, N_2, and Ca^{2+} and rare C_2H_6, SO_4^{2-}, and K^+.
7. The fluid inclusion data indicate that the stibnite mineralization occurred under low temperature (215–336 °C) and pressure (9–14 MPa, equivalent to 0.9–1.4 km deep) in low-salinity ore fluids (3.4–6.9 wt.% NaCl equiv.), conditions typical of epizonogenic-type mineralization (Chen, 2006, 2013).
8. The S and Pb isotope signatures show that the ore-forming elements were mainly sourced from the Palaeozoic strata.

Based on these features, we conclude that the Atebayue Hg—Sb deposit is best classified as epizonogenic type.

6.2 | Tectonic setting and metallogenic model

The South Tianshan Hg—Sb deposits are commonly accompanied with Au, Ba, Ag, and Pb—Zn mineralization, such as the Sawayaerdun (quartz Rb—Sr: 241–231 Ma; Chen & Li, 2003; Ye, Wang, Ye, Li, & Zhang, 1999) and Kalajiaoguya Sb—Au deposits (Chen, Chen, & Baker, 2012a, 2012b; Ni, Man, Hu, Wang, & Sun, 2004), the Bulong Ba—Au deposit (quartz Rb—Sr: 258 ± 15 Ma; Zhao, Yang, Wang, & Yao, 2002; Yang et al., 2006), the Chahansala Ag—Sb deposit (Yang, Wang, Ye, & Chen, 2002; Ye, Wu et al., 1999), and the Huoshibulake Pb—Zn deposit (Rb—Sr: 265 ± 12 Ma; Li & Chen, 2004; Li, Xue et al., 2010; Ye,

Wu et al., 1999). Furthermore, Yao et al. (2015) reported K—Ar ages of 230–236 Ma and 244–268 Ma for two sericite separates from the Haydarkan Hg—Sb deposit.

These published geochronological data constrain the regional Sb polymetallic mineralization to the Early Permian–Middle Triassic (Chen et al., 2012a, 2012b; Yakubchuk, Cole, Seltmann, & Shatov, 2002; Yang et al., 2006; Yao et al., 2015), a time broadly coeval with the Tarim–Kazakhstan continent–continent collision (Chen et al., 2012a, 2012b).

The crustal continuum model is widely used to interpret the genesis and spatial distribution of structurally-controlled lode deposits formed in collisional/accretionary orogeny (Figure 12; Chen & Fu, 1992; Chen, 2013; Goldfarb, Newberry, Pickthorn, & Gent, 1991, Goldfarb et al., 2014; Groves et al., 1998) and is also applicable for the Atebashi-Inylchek Fault-controlled Atebayue Sb deposit (Figures 1b,c and 2). The mineralization depth at Atebayue was likely shallow (<2 km). The mineralization fluids were probably derived from epizonogenic to metamorphic devolatilisation of the Silurian–Permian strata at the footfall of the Atebashi-Inylchek Fault. The fluids may have ascended along the Atebashi-Inylchek Fault and deposited the metals in structural traps (Figure 12).

6.3 | Comparisons with other Hg—Sb belts

Atebayue is representative of the South Tianshan Sb deposits and is similar to many Hg—Sb deposits in the Qinling fold belt (Chen & Santosh, 2014; Chen, Santosh, Somerville, & Chen, 2014), such as the Gongguan and Qingtonggou Hg—Sb deposits (Zhang, Tang et al., 2014). The South Tianshan Hg—Sb belt, combined with the Qinling Hg—Sb belt, is the world's third largest Hg—Sb metallogenic province following the Circum-Pacific Rim and Mediterranean orogenic belts (Ding, 1986).

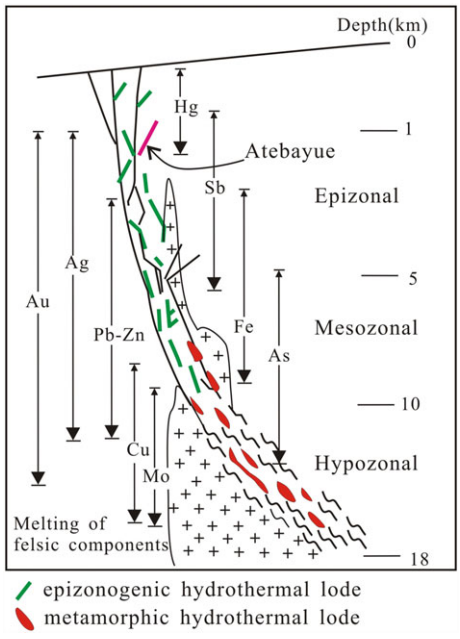

FIGURE 12 Genetic model showing crustal continuum for fault-controlled lode deposits (modified after Chen, 2006, 2013) [Colour figure can be viewed at wileyonlinelibrary.com]

Compared to the latter, two Hg—Sb provinces, the South Tianshan-Qinling Hg—Sb belts have the following unique features (He, Han, An, & Yan, 1996; Zhang, Chen, Hu, Zhang, & Li, 2014; Zhang, Li, Gilbert, Liu, & Shi, 2014; Zhang, Tang et al., 2014): (a) The deposits were developed in an intracontinental setting, rather than plate boundaries; (b) Mineralization generally occurs in the Late Paleozoic to Early Mesozoic, rather than in Cenozoic rocks; (c) Occurrence of stratabound orebodies in sedimentary sequences; (d) The deposits are strictly controlled by brittle faults; and (e) Coexistence of Hg and Sb mineralization and commonly also with Au. For instance, Kyrgyzstan contains the Nichkesu, Severny Aktash, and Savoyardy Sb—Au deposits (Yao et al., 2015). In addition, the Sawayaerdun and Kalajiaoguya Sb—Au were discovered in the southwestern Chinese Tianshan (Xinjiang, NW China; Chen et al., 2012a, 2012b; Yang et al., 2004; Ye, Wu et al., 1999).

6.4 | Mineralization potential

Apart from large Hg—Sb deposits, many world-class orogenic Au deposits were also discovered in the western part of the South Tianshan. For instance, the Muruntau deposit (>5,200 t Au) is the world's second largest gold deposit after Witwatersrand. Moreover, less well-documented orogenic gold deposits (e.g., Tuoguoluoke and Jiangjiaerte) occur further east in South Tianshan (Goldfarb et al., 2014). The gold mineralization potential of these Hg—Sb resources is unclear, but we suggest that the area has considerable potential formed with a synchronously and cogenetically metallogenic event in the western part of South Tianshan (Chen, Zhou et al., 2012c). This inference is supported by the crustal continuum model in collisional orogeny (Figure 12; Chen, 2006, 2013).

7 | CONCLUDING REMARKS

1. The Atebayue Sb deposit is fault controlled and hosted in the Silurian clastics. The ores display epizonal features including vuggy and drusy structures and open-space filling and geodes. The mineral assemblage is dominated by low-temperature hydrothermal stibnite, quartz, and calcite.
2. Only aqueous inclusions are identified in the hydrothermal quartz. The ore-fluids were featured by having low temperature and low salinity. The estimated mineralization pressure was 9–14 MPa, suggesting an ore formation depth of 0.9–1.4 km. The ore-forming materials may have derived mainly from the Palaeozoic strata.
3. The Atebayue Sb deposit is best classified to be epizonogenic type related to tectonic–metallogenic event led by the Late Palaeozoic Tarim–Kazakhstan continent–continent collision.

ACKNOWLEDGEMENTS

This work was jointly granted by the National Natural Science Foundation of China (U1403292 and 41402061), National Key Technology Research and Development Program of the Ministry of Science and Technology of China (2015BAB05B04), Scientific Research Fund

of the Institute of Geomechanics, CAGS (DZLXJK201606), and the China Geological Survey Bureau (1212011120335 and 12120114006201). Careful corrections, relevant comments, and constructive suggestions from an anonymous reviewer and Professor Ian D. Somerville greatly improved our knowledge and the quality of our paper.

REFERENCES

Bai, H. S., & Zhu, J. X. (1984). Geological report of the Gongguan Hg-Sb deposit in Xunyang area, Shaanxi Province. *Unpublished document*, 1–66 (in Chinese).

Belousov, V. I. (2002). Ore-clastic olistostromes, ore clasts, and allochthonous antimony-mercury deposits in the Alay range, southern Tien Shan. *Lithology and Mineral Resources*, *37*, 251–265.

Bodnar, R. J. (1993). Revised equation and table for determining the freezing point depression of H_2O-NaCl solutions. *Geochimica et Cosmochimica Acta*, *57*, 683–684.

Bouzari, F., & Clark, A. H. (2006). Prograde evolution and geothermal affinities of a major porphyry copper deposit: The Cerro Colorado hypogene protore, I Región, northern Chile. *Economic Geology*, *101*, 95–134.

Chen, F. W., & Li, H. Q. (2003). Metallogenic chronology of the Sawayaerdun gold-antimony deposit in Xinjiang. *Acta Geoscientica Sinica*, *24*, 563–567 (in Chinese with English abstract).

Chen, H. Y., Chen, Y. J., & Baker, M. J. (2012a). Evolution of ore-forming fluids in the Sawayaerdun gold deposit in the southwestern Chinese Tianshan metallogenic belt, Northwest China. *Journal of Asian Earth Sciences*, *49*, 131–144.

Chen, H. Y., Chen, Y. J., & Baker, M. J. (2012b). Isotopic geochemistry of the Sawayaerdun orogenic-type gold deposit, Tianshan, northwest China: Implications for ore genesis and mineral exploration. *Chemical Geology*, *310-311*, 1–11.

Chen, Y. J. (2006). Orogenic-type deposits and their metallogenic model and exploration potential. *Geology in China*, *33*, 1181–1196 (in Chinese with English abstract).

Chen, Y. J. (2010). On epizonogenism and genetic classification of hydrothermal deposits. *Earth Science Frontiers*, *17*, 27–34 (in Chinese with English abstract).

Chen, Y. J. (2013). The development of continental collision metallogeny and its application. *Acta Petrologica Sinica*, *29*, 1–17 (in Chinese with English abstract).

Chen, Y. J., & Fu, S. G. (1992). *Gold mineralization in West Henan, China* (pp. 1–234). Beijing: Seismological Press (in Chinese with English abstract).

Chen, Y. J., Ni, P., Fan, H. R., Pirajno, F., Lai, Y., Su, W. C., & Zhang, H. (2007). Diagnostic fluid inclusion of different types hydrothermal gold deposits. *Acta Petrologica Sinica*, *23*, 2085–2108 (in Chinese with English abstract).

Chen, Y. J., & Santosh, M. (2014). Triassic tectonics and mineral systems in the Qinling Orogen, central China. *Geological Journal*, *49*, 338–358.

Chen, Y. J., Santosh, M., Somerville, I. D., & Chen, H. Y. (2014). Indosinian tectonics and mineral systems in China: An introduction. *Geological Journal*, *49*, 331–337.

Chen, Z., & Jing, Z. (2012). The distribution and exploitation situation of preponderant mineral resources in the five countries in central Asia. *Natural Resource Economics of China*, *5*, 34–39 (in Chinese with English abstract).

Chen, Z. L., Zhou, Y. G., Han, F. B., Chen, B. L., Hao, R. X., Li, S. B., & Liu, Z. R. (2012c). Exhumation degree of the Tianshan range and its implications for ore preservation. *Earth Science - Journal of China University of Geosciences*, *37*, 903–916 (in Chinese with English abstract).

Ding, K. (1986). Geochemistry study on the Hg-Sb deposit in Xunyang area, Shaanxi Province. Ph.D. Thesis, Institute of Geochemistry, Chinese Academy of Sciences, Guiyang, 126 pp. (in Chinese).

Goldfarb, R. J., Newberry, R. J., Pickthorn, W. J., & Gent, C. A. (1991). Oxygen, hydrogen, and sulphur isotope studies in the Juneau gold deposit, southeastern Alaska: Constraints on the origin of hydrothermal fluids. *Economic Geology*, *86*, 66–80.

Goldfarb, R. J., Taylor, R. D., Collins, G. S., Goryachev, N. A., & Orlandini, O. F. (2014). Phanerozoic continental growth and gold metallogeny of Asia. *Gondwana Research*, *25*, 48–102.

Groves, D. I., Goldfarb, R. J., Gebre-Mariam, M., Hagemann, S. G., & Robert, F. (1998). Orogenic gold deposits: A proposed classification in the context of their crustal distribution and relationship to other gold deposit types. *Ore Geology Reviews*, *13*, 7–27.

He, L. X., Han, Z. J., An, S. R., & Yan, J. P. (1996). *The geology of mercury deposit and the reconnaissance survey and exploration*. Beijing: Geological Publishing House, 129pp. (in Chinese with English abstract).

Hoefs, J. (1997). *Stable isotope geochemistry* (4th ed.). (pp. 201). Berlin: Springer-Verlag.

Li, H. H., Qiu, R. Z., Tan, Y. J., Qi, S. j., Wang, Q. M., Wang, K. A., … Han, J. X. (2010). *The exploration and development guidelines of mineral resources in the five countries in central Asian* (pp. 207). Wuhai: China University of Geosciences Press (in Chinese).

Li, H. Q., & Chen, F. W. (2004). *Isotopic geochronology of regional mineralization in Xinjiang, China* (pp. 391). Beijing: Geological Publishing House (in Chinese with English abstract).

Li, Z. D., Xue, C. J., Zhang, S., Shi, H. G., & Wang, S. C. (2010). Geology, geochemistry and genesis of Huoshibulake Zn-Pb deposit in south-western Tianshan, Xinjiang. *Mineral Deposits*, *29*, 983–998 (in Chinese with English abstract).

Ni, S. B., Man, F. S., Hu, S. L., Wang, Z. R., & Sun, X. (2004). Determination of the age of ore-bearing strata and ore forming age of the Kalajiaoguya Sb-Au ore deposit in Tianshan Mountains of Xinjiang in China. *Journal of University of Science and Technology of China*, *34*, 342–347 (in Chinese with English abstract).

Osmonbetov, K. O. (1986). *Antimony deposits, Kyrgyzstan* (pp. 206). Flunze: Ilim Press (in Russia).

Pirajno, F. (2009). *Hydrothermal processes and mineral system* (pp. 1250). Berlin: Springer.

Robinson, B. W., & Kusakabe, M. (1975). Quantitative preparation of sulphur dioxide, for $^{34}S/^{32}S$ analyses, from sulphides by combustion with cuprous oxide. *Analytical Chemistry*, *47*, 1179–1181.

Sasaki, A., & Krouse, H. R. (1969). Sulphur isotopes and the Pine Point lead-zinc mineralisation. *Economic Geology*, *64*, 718–730.

Sengör, A. M. C., Natalin, B. A., & Burtman, V. S. (1993). Evolution of the Altaid tectonic collage and Palaeozoic crustal growth in Eurasia. *Nature*, *364*, 299–307.

Todt, W., Cliff, R. A., Hanser, A., & Hofmann, A. W. (1993). Re-calibration of NBS lead standards using a $^{202}Pb+^{205}$ Pb double spike. Terra abstract p. 396.

Tu, G. Z. (1998). *Low-temperature geochemistry*. Beijing: Science Press, 266pp. (in Chinese).

Wang, H., Jin, C. Z., Bao, Q. Z., Sha, D. M., & Hu, X. J. (2003). The preliminary study of the geological character and origin for Chahanshala Sb deposit. *Geology and Prospecting*, *39*, 26–30 (in Chinese with English abstract).

Xue, C. J., Zhao, X. B., Mo, X. X., Chen, Y. C., Dong, L. H., Gu, X. X., … Liu, J. Y. (2014). Tectonic-metallogenic evolution of western Tianshan giant Au-Cu-Zn-Pb metallogenic belt and prospecting orientation. *Acta Geologica Sinica*, *88*, 2490–2531 (in Chinese with English abstract).

Yakubchuk, A., Cole, A., Seltmann, R., & Shatov, V. (2002). Tectonic setting, characteristics, and regional exploration criteria for gold mineralization in the Altaid orogenic collage: The Tien Shan province as a key example. *Society of Economic Geologists Special Publication*, *9*, 177–201.

Yang, F. Q., Mao, J. W., Wang, Y. T., & Bierlein, F. P. (2006). Geology and geochemistry of the Bulong quartz-barite vein-type gold deposit in the Xinjiang Uygur autonomous region, China. *Ore Geology Reviews*, *29*, 52–76.

Yang, F. Q., Wang, L. B., Wang, Y. T., Xia, H. D., Deng, H. J., & Ma, B. Y. (2004). Ore-forming prospects of gold-antimony metallogenic belt in

south-western Tianshan Mountain of Xinjiang, China. *Journal of Chengdu University of Technology*, *31*, 338–344 (in Chinese with English abstract).

Yang, F. Q., Wang, L. B., Ye, Q. T., & Chen, M. Y. (2002). Types of antimony deposits and characteristics of the typical deposits in southwest Tianshan Mountains. *Journal of Chengdu University of Technology*, *29*, 545–550 (in Chinese with English abstract).

Yang, Z. H. (1991). *Tectonic-lithofacies and metallogeny of marginal transform basin* (pp. 228). Beijing: Science Press (in Chinese).

Yao, W. G., Lv, P. R., Wu, L., Hong, J., Yang, B., Jia, Q. Z., & Li, B. Q. (2015). Geological characteristics of dominant mineral resources of the Tianshan Mountains in Kyrgyzstan and their prospecting potential. *Geological Bulletin of China*, *34*, 710–725 (in Chinese with English abstract).

Ye, J., Wang, L., Ye, Q., Li, H., & Zhang, X. (1999). Metallogenic epoch and ore-bearing strata age of the Sawaya'erdun gold-antimony deposit in Tianshan Mountains, China. *Acta Geoscientia Sinica*, *20*, 278–283 (in Chinese with English abstract).

Ye, Q. T., Wu, Y. P., Fu, X. J., Chen, M. Y., Ye, J. H., Zhuang, D. Z., … Bai, H. H. (1999). *Ore-forming conditions and metallogenic prognosis of gold and non-ferrous metallic resources in south-western Tianshan Mountain* (pp. 201). Beijing: Geological Publishing House (in Chinese with English abstract).

Zartman, R. E., & Doe, B. R. (1981). Plumbotectonics–the model. *Tectonophysics*, *75*, 135–162.

Zhang, J., Li, L., Gilbert, S., Liu, J. J., & Shi, W. S. (2014). LA-ICP-MS and EPMA studies on the Fe-As-S minerals from the Jinlongshan gold deposit, Qinling Orogen, China: Implications for ore-forming processes. *Geological Journal*, *49*, 482–500.

Zhang, Y., Tang, H. S., Chen, Y. J., Leng, C. B., & Zhao, C. H. (2014). Ore geology, fluid inclusion and isotope geochemistry of the Xunyang Hg–Sb orefield, Qinling Orogen, central China. *Geological Journal*, *49*, 463–481.

Zhang, Z. J., Chen, H. Y., Hu, M. Y., Zhang, J., & Li, D. F. (2014). Isotopic geochemistry of the Jinwozi gold deposit in the eastern Tianshan orogen, Northwest China: Implications for the ore genesis. *Geological Journal*, *49*, 574–583.

Zhao, R. F., Yang, J. G., Wang, M. C., & Yao, W. G. (2002). The study of metallogenic geologic setting and prospecting potential evaluation in south-western Tianshan Mountains. *North-western Geology*, *35*, 101–121 (in Chinese with English abstract).

Zhu, X. Y., Wang, J. B., Liu, Z. R., & Fang, T. H. (2010). Geologic characteristics and the genesis of the Wulagen lead-zinc deposit, Xinjiang, China. *Acta Geologica Sinica*, *84*, 694–702 (in Chinese with English abstract).

How to cite this article: Zhou Z, Chen Z, Han F, et al. Fluid inclusion and isotope geochemistry of the Atebayue Sb deposit, South Tianshan Orogen, Kyrgyzstan. *Geological Journal*. 2017. https://doi.org/10.1002/gj.2943